photonics

MDPI

Communication

Axial Resolution Enhancement of Optical Sectioning Structured Illumination Microscopy Based on Three-Beam Interference

Chao Xiao [1,2], Xing Li [1,2], Jia Qian [1], Wang Ma [1,2], Junwei Min [1,2], Peng Gao [3], Dan Dan [1,2,*] and Baoli Yao [1,2,*]

[1] State Key Laboratory of Transient Optics and Photonics, Xi'an Institute of Optics and Precision Mechanics, Chinese Academy of Sciences, Xi'an 710119, China
[2] University of Chinese Academy of Sciences, Beijing 100049, China
[3] School of Physics, Xidian University, Xi'an 710071, China
* Correspondence: dandan@opt.ac.cn (D.D.); yaobl@opt.ac.cn (B.Y.)

Abstract: As a branch of 3D microscopy, optical sectioning structured illumination microscopy (OS-SIM) has the advantages of fast imaging speed, weak photobleaching and phototoxicity, and flexible and compatible configuration. Although the method of using the one-dimensional periodic fringe pattern projected on the sample can remove the out-of-focus background from the in-focus signal, the axial resolution of the final reconstructed 3D image is not improved. Here, we propose a three-beam interference OS-SIM, namely TBOS, instead of the common-used dual-beam interference OS-SIM (DBOS). The three-beam interference scheme has been adopted in 3D super-resolution SIM (3D-SR-SIM), where the fringe phase shifting needs to be along each of the three orientations. In contrast, TBOS applies phase shifting only in one arbitrary direction. We built a TBOS SIM microscope and performed the 3D imaging experiments with 46 nm diameter fluorescent microspheres and a mouse kidney section. The axial resolution of the 3D image obtained with TBOS was enhanced by a factor of 1.36 compared to the DBOS method, consistent with the theoretical analysis and simulation. The OS-SIM with enhanced axial resolution for 3D imaging may find a wide range of applications in the biomedical field.

Keywords: structured illumination microscopy; optical sectioning; three-beam interference; axial resolution; 3D microscopy

check for updates

Citation: Xiao, C.; Li, X.; Qian, J.; Ma, W.; Min, J.; Gao, P.; Dan, D.; Yao, B. Axial Resolution Enhancement of Optical Sectioning Structured Illumination Microscopy Based on Three-Beam Interference. *Photonics* **2023**, *10*, 682. https://doi.org/10.3390/photonics10060682

Received: 11 May 2023
Revised: 28 May 2023
Accepted: 9 June 2023
Published: 12 June 2023

Copyright: © 2023 by the authors. Licensee MDPI, Basel, Switzerland. This article is an open access article distributed under the terms and conditions of the Creative Commons Attribution (CC BY) license (https://creativecommons.org/licenses/by/4.0/).

1. Introduction

Optical microscopes are ubiquitous in biomedical research for observing cell and tissue structures and their dynamic events [1,2]. However, due to the limited depth-of-field (DOF) of the objective lens, the in-focus target and out-of-focus background components of the samples are mixed in the recorded image [3], which leads to a low contrast and low signal-to-background ratio in the image, further restricting the ability of 3D imaging of optical microscopy [4,5]. The key to overcoming this drawback of 3D microscopic imaging is to extract the in-focus information from the out-of-focus background to obtain optical sectioning images. The laser scanning confocal microscopy (LSCM) [6,7], two-photon microscopy (TPM) [8,9], light sheet fluorescence microscopy (LSFM) [10,11], and optical sectioning structured illumination microscopy (OS-SIM) [12,13] are the mostly often used methods for this goal.

The pointwise scanning scheme of optical sectioning imaging adopted by LSCM and TPM intrinsically has slow imaging speed [14]. The LSFM, with the alias of selective or single plane illumination microscopy (SPIM) [15], employs two orthogonally arranged objective lenses to excite and detect transparent samples [16,17], which is elegant but complex and expensive to use. In contrast, the OS-SIM is built on a conventional wide-field microscope by replacing the Koehler illumination with a fringe-structured illumination, making the OS-SIM more accessible and affordable.

The principle of OS-SIM is based on the dependence of the projected fringe modulation on the depth of field, that is, the illuminating fringe pattern only has a high modulation depth in the in-focus plane while it decays rapidly in the out-of-focus region [18]. Through three rounds of equilateral phase shifting of the fringe, and the Mean-Square-Root (RMS) reconstruction algorithm [12], the out-of-focus background and the fringe imposed on the in-focus component can be removed, resulting in a sectioned image of the sample. With axial scanning of the sample, a sequentially sectioned image stack can be obtained and a 3D rendering object can be visualized using software. Though OS-SIM can remove the out-of-focus background, it does not improve the axial resolution in the final 3D-reconstructed image. Three-dimensional super-resolution SIM (3D-SR-SIM) enables the improvement in both axial and lateral resolutions with 3D-structured illumination via three- or four-beam interference [19,20]. However, it generally requires 15 steps of phase shifting, i.e., 5-step phase shifting along each of the three fringe orientations, resulting in a high data capacity and low imaging speed.

In this paper, we propose the three-beam interference scheme for optical sectioning SIM, namely TBOS. It owns the optical sectioning capability with enhanced axial resolution. The axial resolution is improved by 1.36 times compared to the common-used dual-beam interference OS-SIM (named DBOS). The phase-shifting step is only one third of the 3D-SR-SIM, benefiting from its phase-shifting operation only along one spatial orientation. The feasibility and merits of the TBOS method were verified with 3D imaging experiments on 46 nm diameter fluorescent microspheres and a mouse kidney section.

2. Principle of TBOS

Assuming a sample labeled with fluorophores has a spatial density distribution of $S(\boldsymbol{r}, z)$, where $\boldsymbol{r}$ indicates the lateral coordination (x, y) and z represents the axial coordination, the intensity distribution of the structured illumination on the sample is $I(\boldsymbol{r}, z)$. The 3D image $D(\boldsymbol{r}, z)$ can be expressed in the form:

$$D(\boldsymbol{r}, z) = [I(\boldsymbol{r}, z)S(\boldsymbol{r}, z)] \otimes h(\boldsymbol{r}, z), \tag{1}$$

where $h(\boldsymbol{r}, z)$ represents the 3D point spread function (PSF) of the system, and the symbol $\otimes$ denotes the convolution operation. To generate a 3D-structured illumination pattern, three coherent beams are employed for interference. For simplicity, one beam's wave vector is indicated by $\boldsymbol{k}_0$ and propagates along the z-axis, and the other two beams (wave vectors denoted by $\boldsymbol{k}_1$ and $\boldsymbol{k}_{-1}$, respectively) symmetrically transmit along the z-axis at angles of $\pm\theta$ to the xz-plane, as illustrated in Figure 1a. The amplitudes of the three beams are set to identical. Figure 1b shows the 3D intensity distribution of the formed structured illumination with the three-beam interference.

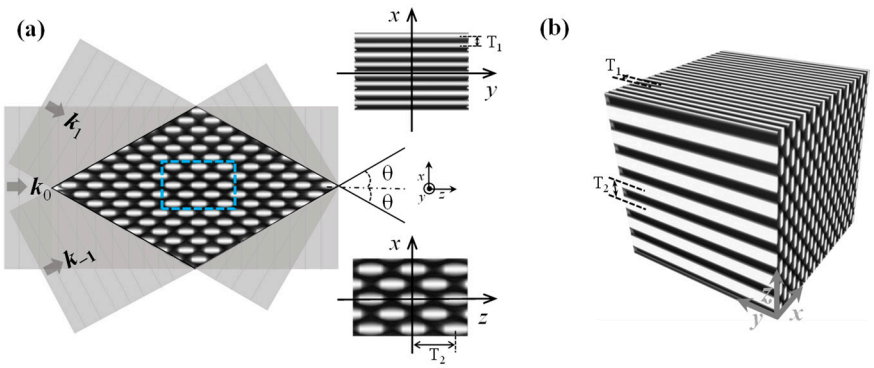

Figure 1. The scheme of three-beam interference. (**a**) The xz-plane patterns generated by three-beam interference. Inset: Enlarged drawing in the blue dashed box; (**b**) the 3D visualization of the pattern.

We further concentrate on the 3D-structured illumination intensity distribution in the *xz*-plane. The conclusion of *xz*-plane imaging is accessible to the *yz*- and *xy*-plane. The intensity distribution of structured illumination in the *xz*-plane is described by:

$$I(x,z) = 1 + \frac{2}{3}\cos(2\pi v_1 x + 2\varphi) + \frac{4}{3}\cos(\pi v_1 x + \varphi)\cos(2\pi v_2 z), \tag{2}$$

here, $v_1 = \frac{1}{T_1} = \frac{2n\sin\theta}{\lambda}$ and $v_2 = \frac{1}{T_2} = \frac{n(1-\cos\theta)}{\lambda}$ denote the spatial frequencies of the interference pattern in the lateral and axial directions, respectively. n is the refractive index of the surrounding medium, λ represents the wavelength of emission light, $\varphi = \varphi_0 + m\Delta\varphi$ denotes the phase of the fringe, φ_0 denotes the initial phase, and $\Delta\varphi$ represents the phase step between consecutive images; m is the order of the phase shifting.

Considering the depth-of-focus of the objective lens, the sample distribution $S(x, z)$ can be divided into two components of the in-focus portion $S_{in}(x, z)$ and the out-of-focus background $S_{out}(x, z)$. Under the structured illumination, only the in-focus $S_{in}(x, z)$ is modulated by the illumination pattern $I(x, z)$. Substituting Equation (2) into Equation (1), we obtain:

$$\begin{aligned} D(x,z) = {} & [S_{in}(x,z) + S_{out}(x,z)] \otimes h(x,z) + \tfrac{2}{3}[\cos(2\pi v_1 x + 2\varphi) S_{in}(x,z)] \otimes h(x,z) \\ & + \tfrac{4}{3}[\cos(\pi v_1 x + \varphi)\cos(2\pi v_2 z) S_{in}(x,z)] \otimes h(x,z). \end{aligned} \tag{3}$$

For the image acquired with a 2D camera, the coordinate z is kept fixed, so, the term of $\cos(2\pi v_2 z)$ can be regarded as a constant. Therefore, Equation (3) can be rewritten as:

$$\begin{aligned} D(x,z) = {} & [S_{in}(x,z) + S_{out}(x,z)] \otimes h(x,z) + \tfrac{2}{3}[\cos(2\pi v_1 x + 2\varphi) S_{in}(x,z)] \otimes h(x,z) \\ & + \tfrac{4}{3}[\cos(\pi v_1 x + \varphi) S_{in}(x,z)] \otimes H(x,z), \end{aligned} \tag{4}$$

where $H(x, z)$ is defined as an equivalent PSF, $H(x,z) = h(x,z)\cos(2\pi v_2 z)$. In Equation (4), the first term represents the wide-field image, composed of the in-focus information $S_{in}(x, z)$ and the out-of-focus background $S_{out}(x, z)$. The second and third terms imply the sectioned image, which only includes the $S_{in}(x, z)$, but noting the PSF $h(x, z)$ of the third convolution is replaced by $H(x, z)$ modulated by $\cos(2\pi v_2 z)$.

The equivalent PSF $H(x, z)$ is determined by the parameters of both the optical system and the illumination pattern, which is consequently compressed due to the cosine modulation. To prove this quantitatively, we use the system's theoretical PSF $h(x,z) = \mathrm{Sinc}^2\left[kn\sin^2(\alpha/2)(x,z)\right]$ [21] in $H(x, z)$. Here, $k = 2\pi/\lambda$, n denotes the surrounding refractive index, and α represents the aperture angle of the objective lens. The $\cos(2\pi v_2 z)$ is modulated by the axial frequency v_2, which has a relationship with the lateral frequency v_1:

$$v_2 = \frac{n\left\{1 - \cos\left[\arcsin(\frac{\lambda}{2n} v_1)\right]\right\}}{\lambda}. \tag{5}$$

To maintain consistency with the afterward experimental conditions, we select the wavelength λ = 560 nm, and an oil-immersion objective lens of 60×/NA1.49 matching n = 1.515. The dashed curve in Figure 2a presents the system's axial PSF $h(x, z)$, where $z = 0$ indicates the axial location of the transverse in-focus plane. The equivalent PSFs $H(x, z)$ corresponding to different v_1 are also plotted in Figure 2a. It can be seen that the full width at half maximum (FWHM) of $H(x, z)$ is smaller than that of $h(x, z)$, which means the axial resolution is improved. However, the intensity of the side lobes of $H(x, z)$ gradually increases with the increase of v_1, which will affect the final reconstructed image quality and even lead to artifacts. According to the previous research [18] that indicates a maximal optical sectioning strength obtained around v_1 = 0.5, as shown in Figure 2b, we select v_1 = 0.6 to obtain the optimized axial resolution enhancement and minimized influence of the side lobes in practice. In this case, the FWHMs of $h(x, z)$ and $H(x, z)$ are 0.677 μm and 0.483 μm, respectively, corresponding to an axial resolution improved by 1.4 times.

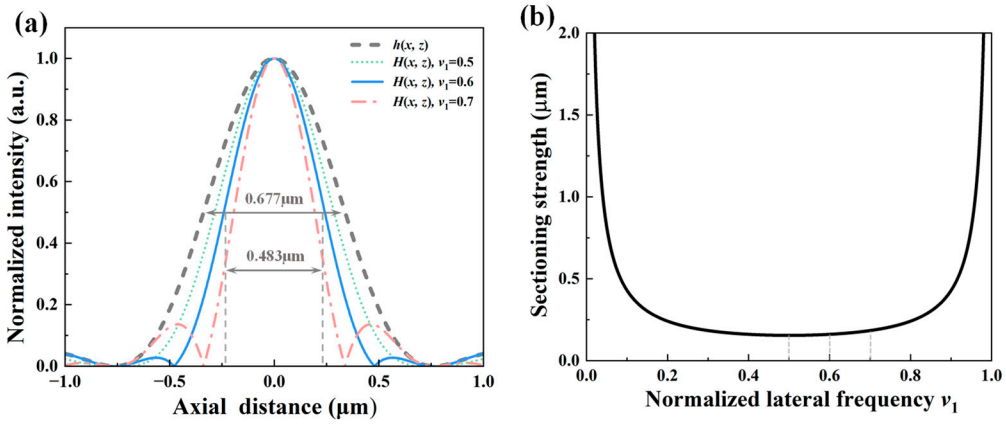

Figure 2. (**a**) Simulations of the axial PSFs at different normalized lateral frequency v_1; (**b**) the relationship of the optical sectioning strength with the v_1.

To obtain the sectioned image with improved axial resolution, in Equation (4), we set:

$$\begin{cases} g_w = [S_{in}(x,z) + S_{out}(x,z)] \otimes h(x,z) \\ g_c = \frac{2}{3}[\cos(2\pi v_1 x + 2\varphi_0) S_{in}(x,z)] \otimes h(x,z) \\ g_s = -\frac{2}{3}[\sin(2\pi v_1 x + 2\varphi_0) S_{in}(x,z)] \otimes h(x,z) \\ q_c = \frac{4}{3}[\cos(\pi v_1 x + \varphi_0) S_{in}(x,z)] \otimes H(x,z) \\ q_s = -\frac{4}{3}[\sin(\pi v_1 x + \varphi_0) S_{in}(x,z)] \otimes H(x,z) \end{cases}. \quad (6)$$

Then, Equation (4) becomes a simplified form:

$$D(x,z) = g_w + g_c \cos(2m\Delta\varphi) + g_s \sin(2m\Delta\varphi) + q_c \cos(m\Delta\varphi) + q_s \sin(m\Delta\varphi). \quad (7)$$

To solve the five unknown parameters of g_w, g_c, g_s, q_c, and q_s, it requires five equations, which can be created by setting the phase difference $\Delta\varphi = \frac{2}{5}\pi$ and the order of phase shifting m = 0, 1, 2, 3, 4. Then, we obtain the following equation group:

$$\begin{bmatrix} D_0(x,z) \\ D_1(x,z) \\ D_2(x,z) \\ D_3(x,z) \\ D_4(x,z) \end{bmatrix} = \begin{bmatrix} 1 & 1 & 0 & 1 & 0 \\ 1 & \cos\frac{4}{5}\pi & \sin\frac{4}{5}\pi & \cos\frac{2}{5}\pi & \sin\frac{2}{5}\pi \\ 1 & \cos\frac{8}{5}\pi & \sin\frac{8}{5}\pi & \cos\frac{4}{5}\pi & \sin\frac{4}{5}\pi \\ 1 & \cos\frac{12}{5}\pi & \sin\frac{12}{5}\pi & \cos\frac{6}{5}\pi & \sin\frac{6}{5}\pi \\ 1 & \cos\frac{16}{5}\pi & \sin\frac{16}{5}\pi & \cos\frac{8}{5}\pi & \sin\frac{8}{5}\pi \end{bmatrix} \begin{bmatrix} g_w \\ g_c \\ g_s \\ q_c \\ q_s \end{bmatrix}. \quad (8)$$

By solving Equation (8), we obtain g_w, g_c, g_s, q_c, and q_s, and then we can calculate the optical sectioned image for TBOS with the following equation:

$$D_{\mathrm{TBOS}}(x,z) = \sqrt{{q_c}^2 + {q_s}^2}. \quad (9)$$

It is noticed that this formula is similar to the amplitude demodulation algorithm for the two-beam optical sectioning SIM [22,23], that is $\propto \sqrt{{g_c}^2 + {g_s}^2}$. However, here we obtain an improved axial resolution OS image with Equation (9) due to the compressed PSF $H(x, z)$.

3. Simulation Results

Numerical simulation is performed at first to validate the superiority of TBOS, than DBOS, in axial resolution. The standard USAF1951 resolution chart is used as the simulated object, as shown in Figure 3a. For DBOS, three-step phase shifting with an interval of $2\pi/3$ is conducted, and the optical sectioning image is reconstructed according to the conventional RMS algorithm, shown in Figure 3c. In addition, the wide-field image can also be obtained by summing up the three raw images, shown in Figure 3b. For TBOS, five-step phase shifting with an interval of $2\pi/5$ is conducted, and the optical sectioning

image is reconstructed according to Equations (8) and (9), shown in Figure 3d. It is clear that the TBOS image is much sharper than the DBOS image. Elements 9–6 corresponding to a spatial frequency of 912.3 lp/mm in the TBOS image can be clearly resolved, while they are blurred for the DBOS image. The normalized intensity profiles in Figure 3i along the same cut-lines of Figure 3e–h support the axial resolution improvement of TBOS over the DBOS.

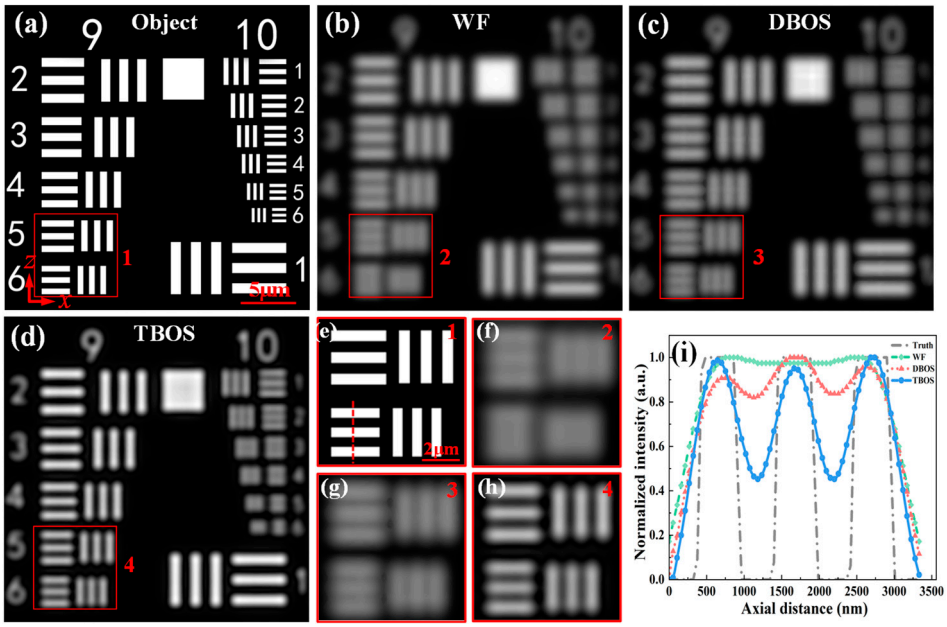

Figure 3. Comparison of simulated reconstructed images in *xz*-plane by different methods. (**a**) The ground truth; (**b**) the wide-field image; (**c**) the reconstructed image with the DBOS method; (**d**) the reconstructed image with the TBOS method; (**e**–**h**) enlarged views of the red boxes 1, 2, 3, and 4 in (**a**–**d**), respectively; and (**i**) normalized intensity profiles along the red dotted lines in (**e**–**h**).

We also compare the lateral resolving powers of TBOS and DBOS in the *xy*-plane. Similarly, the USAF1951 resolution chart is used as the target, as shown in Figure 4a. The reconstructed wide-field image, DBOS image, and TBOS image are shown in Figure 4b–d, respectively. It can be seen that the TBOS image and the DBOS image have a similar resolving power, while the imaging contrast of the DBOS is a little bit higher than the TBOS, seen from the zoomed regions (elements 11–3 and 11–4) in Figure 4e–h and the normalized intensity profiles in Figure 4i. The reason is because the lateral frequency of the fringe is $v_1/2$ in the case of TBOS, which is half of that of the DBOS ($v_1 = 0.6$), therefore causing a lower optical sectioning capability than the DBOS in the lateral direction. Nevertheless, the difference is not remarkable as seen from the optical sectioning strength curve of Figure 2b.

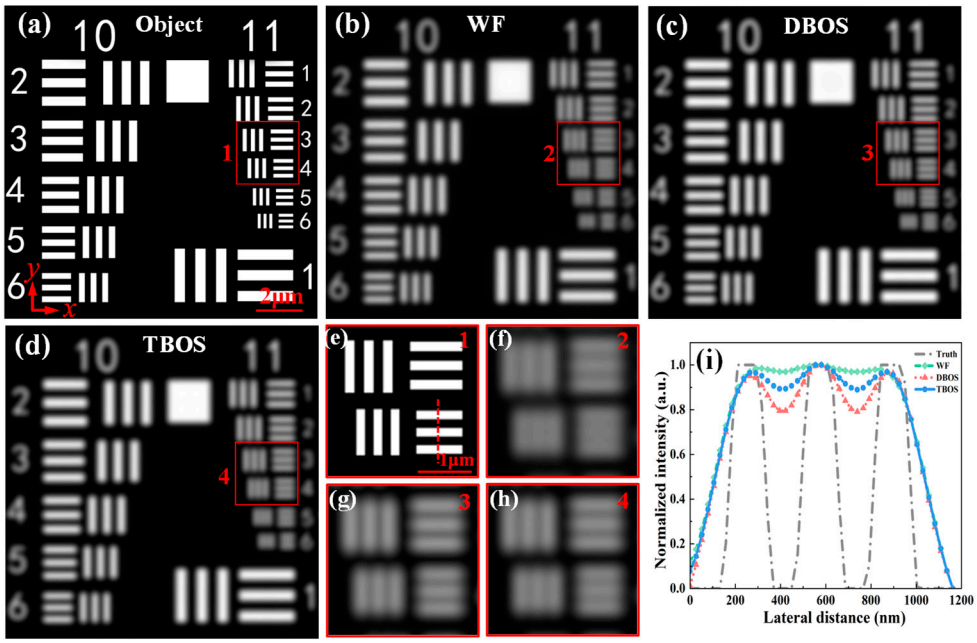

Figure 4. Comparison of simulated reconstructed images in *xy*-plane by different methods. (**a**) The ground truth; (**b**) the wide-field image; (**c**) the reconstructed image with the DBOS method; (**d**) the reconstructed image with the TBOS method; (**e**–**h**) enlarged views of the red boxes 1, 2, 3, and 4 in (**a**–**d**), respectively; and (**i**) normalized intensity profiles along the red dotted lines in (**e**–**h**).

4. Experimental Results and Discussion

4.1. Experimental Setup

The TBOS SIM microscope was built to verify the theory and simulation results. The optical layout of the setup is illustrated in Figure 5. A laser beam (λ = 473 nm) with horizontally linear polarization (GEM473, Laser Quantum Inc., Stockport, UK) is expanded by Lens 1 (f_1 = 10 mm) and Lens 2 (f_2 = 250 mm), and then illuminates a ferroelectric liquid crystal spatial light modulator (FLC-SLM; QXGA-3DM, 2048 × 1536 pixels, Forth Dimension Displays Inc., Dalgety Bay, UK) through a polarizing beam splitter (PBS) and a half-wave plate (HWP). The FLC-SLM can rapidly generate and shift the diffractive gratings displayed on it, dividing the laser beam into multiple diffraction beams. The 0th and ±1st order diffraction beams are selected by a spatial filter in the focal plane of Lens 3 (f_3 = 500 mm), and then relayed by a 4f system consisting of Lens 4 (f_4 = 175 mm) and Lens 5 (f_5 = 125 mm) to the back focal plane of the objective lens (Apo TIRF, 60×/NA1.49, Nikon Inc., Tokyo, Japan). The 3D-structured illumination pattern is generated in the focal region of the objective lens via the three-beam interference. The sample is mounted on an assembly motorized XY and piezo Z-axis translation stage (XY, PZ-2000FT; Z, PZ-2500FT, Applied Scientific Instrumentation Inc., Eugene, OR, USA). The fluorescence signal is filtered by a dichroic beamsplitter (Di03-R488/561, Semrock Inc., Rochester, NY, USA) and an emission filter (FF01-523/610-25, Semrock Inc., Rochester, NY, USA), and then collected by a tube lens (f = 300 mm) and imaged on the sCMOS camera (C11440-22CU, 2048 × 2048 pixels, maximum 100fps, Hamamatsu Inc., Hamamatsu, Japan). For comparison, the TBOS SIM microscope can be easily changed to the DBOS SIM configuration by blocking the 0th-order diffraction beam.

4.2. Axial Resolution Measurement

The 46 nm diameter fluorescence bead slide (TransFluoSpheres, carboxylate-modified, Ex.488 nm/Em.560 nm, Thermo Fisher Inc., Waltham, MA, USA) is used to measure the axial resolutions of the TBOS and DBOS systems. The lateral frequency of the fringe is measured to be 3367 lp/mm, and the system's lateral cut-off frequency is $2NA/\lambda = 2 \times 1.49/(560 \times 10^{-6})$

= 5321 lp/mm, thus $v_1 \approx 0.63$. The sample is axially scanned in a range of 4.2 μm with a step of 100 nm.

The maximum intensity projection (MIP) images in the *xy*- and *xz*-plane of the sectioned image stacks for the wide-field, DBOS, and TBOS methods are shown in Figure 6a–c, respectively. We select some sub-volumes (as marked 1, 2, 3) to zoom-in for the detailed comparison, as seen in Figure 6d–i, respectively. To obtain the quantitative value of the lateral and axial resolution of the system, we select 50 beads randomly in the field to measure their lateral and axial FWHMs as shown in Figure 6j,k. After Gaussian fitting and statistics, the average lateral FWHMs for the wide-field, DBOS, and TBOS are 326 ± 21 nm, 303 ± 30 nm, and 288 ± 25 nm, respectively. The average axial FWHMs for those methods are 897 ± 51 nm, 895 ± 46 nm, and 660 ± 47 nm, respectively. The measurements indicate that the DBOS method does not improve the lateral and axial resolution compared to the wide-field microscopy, but the TBOS method does improve the axial resolution by 1.36 times compared with the DBOS and the wide-field microscopy. Through this calibration measurement with fluorescent beads, it is verified that our proposed TBOS method has superiority over the conventional DBOS method in axial resolution, despite the lateral resolution not being improved, implying the 3D imaging capability of the TBOS still has space to be improved.

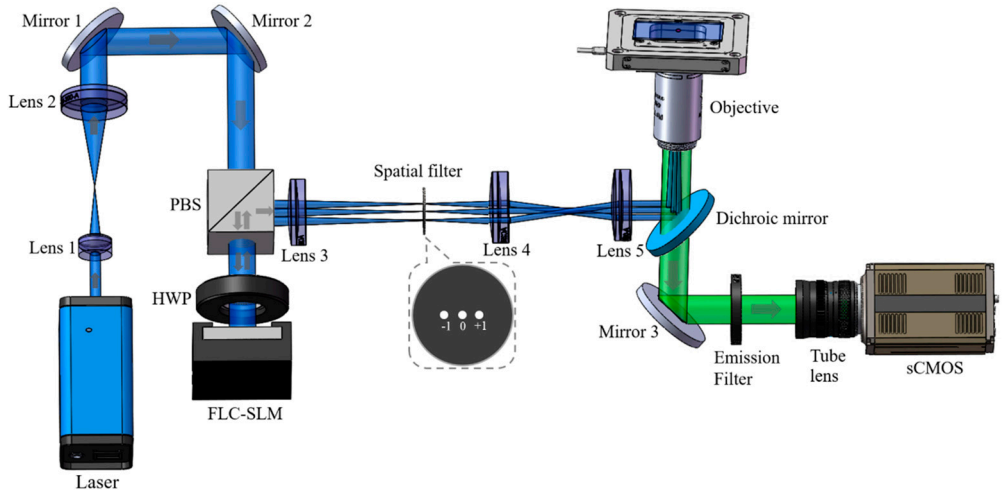

Figure 5. Optical layout of the TBOS SIM microscope. PBS: polarizing beam splitter; HWP: half-wave plate; FLC-SLM: ferroelectric liquid crystal spatial light modulator.

4.3. Imaging Result of Biological Sample

After the resolution calibration with fluorescent beads, a biological specimen of a tri-chrome-labelled mouse kidney section slide (FluoCells prepared slide #3, labelled with Alexa Fluor® 488 WGA, Ex.358 nm/Em.461 nm, Alexa Fluor® 568 phalloidin, Ex.495 nm/Em.519 nm, and DAPI, Ex.578 nm/Em.600 nm, Thermo Fisher Inc., Waltham, MA, USA) is used to test the imaging merit of the TBOS method. The sample is axially scanned in a range of 12.2 μm with a step of 200 nm, generating 62-slice-sectioned images. The MIP images in the *xy*- and *xz*-plane of the stacked image for the wide-field, DBOS, and TBOS methods are shown in the upper and middle rows of Figure 7a–c, respectively. The single cross-section OS images in the *xz*-plane along the white cut-lines in the upper section are also shown in the lower rows of Figure 7a–c, respectively. It is obvious that the TBOS and DBOS images are sharper than the wide-field image, proving that both TBOS and DBOS have the background removal ability. Further, we select some sub-volumes in the specimen (as marked 1, 2, 3) to zoom-in for detailed comparison, as seen in Figure 7d–i, respectively. The TBOS has a better axial resolving power of discrimination of the fine structure of the sample than the DBOS method, which can be seen from the zoomed-in MIP images in the *xz*-plane of Figure 7h,i, and it is more apparent in the normalized intensity

profiles in Figure 7j. The 3D volume visualization of the sample with the different methods is shown in Figure 7k–m, respectively. Through this experiment, it further demonstrates that compared with the wide-field microscopy, both the TBOS and the DBOS methods can remove the out-of-focus background to obtain the optical sectioning image, but the TBOS can further improve the axial resolution rather than the DBOS. Although the influence of the side lobes of PSF on the final reconstructed image quality is the main factor of limiting the 3D imaging capability of TBOS, it is worthy to investigate the way to eliminate the side lobes to further improve the 3D imaging capability.

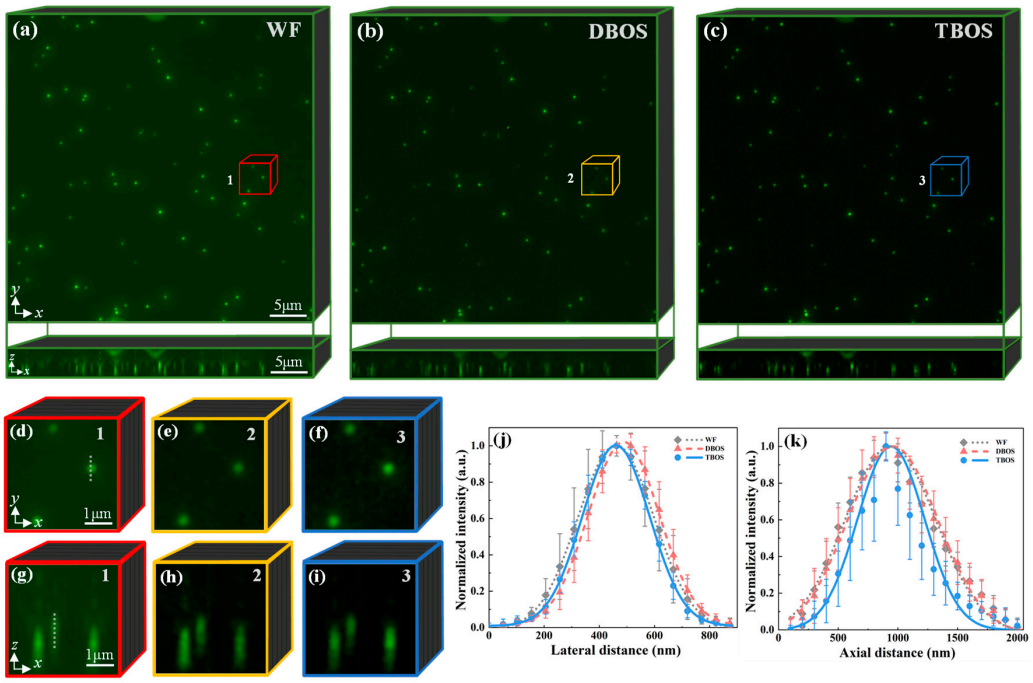

Figure 6. The 3D imaging results of 46 nm diameter fluorescent beads with different methods. (**a**) The wide-field MIP images in *xy*- and *xz*-plane; (**b**) the reconstructed MIP images in *xy*- and *xz*-plane with the DBOS method; (**c**) the reconstructed MIP images in *xy*- and *xz*-plane with the TBOS method; (**d**–**f**) enlarged MIP images in *xy*-plane for the marked colored boxes 1, 2, and 3 in (**a**–**c**), respectively; (**g**–**i**) the MIP images in *xz*-plane of (**d**–**f**), respectively; (**j**) normalized intensity profiles of 50 beads along the lateral direction with Gaussian fitting; and (**k**) normalized intensity profiles of 50 beads along the axial direction with Gaussian fitting.

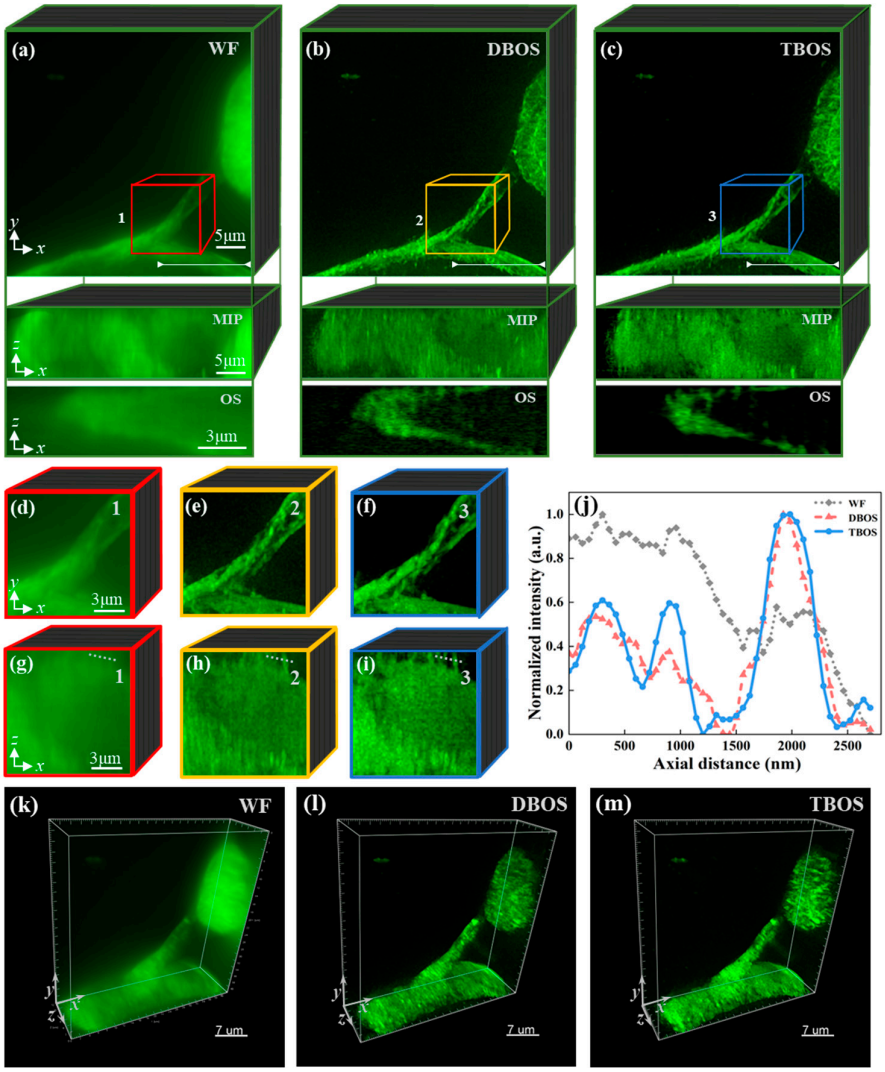

Figure 7. The 3D imaging results of mouse kidney section with different methods. (**a**) The wide-field MIP images in *xy*- and *xz*-plane and the single cross-section OS image in *xz*-plane along the cut-line; (**b**) the MIP images in *xy*- and *xz*-plane and the single cross-section OS image in *xz*-plane with the DBOS method; (**c**) the MIP images in *xy*- and *xz*-plane and the single cross-section OS image in *xz*-plane with the TBOS method; (**d**–**f**) enlarged MIP images in *xy*-plane for the marked colored boxes 1, 2, and 3 in (**a**–**c**), respectively; (**g**–**i**) the MIP images in *xz*-plane of (**d**–**f**), correspondingly; (**j**) normalized intensity profiles along the white dotted lines in (**g**–**i**); and (**k**–**m**) the 3D volume visualization of the sample with the three different methods, respectively.

5. Conclusions

In this work, we have proposed a three-beam interference OS-SIM (TBOS). The theoretical analysis and numerical simulation demonstrated that the TBOS method can improve the axial resolution of the 3D optical section image by 1.4 times compared with the dual-beam interference OS-SIM (DBOS). The experiments with 46 nm diameter fluorescent microspheres and a mouse kidney section further proved that the TBOS method obtained a 1.36-fold improvement in the axial resolution compared to the DBOS method. Though the three-beam interference scheme has been adopted in 3D-SR-SIM, the TBOS method applies phase shifting only in one direction, reducing the raw image amount by a three-fold extent and thus offering a faster 3D imaging speed. We expect the TBOS method to be found in more applications in the biomedical field.

Author Contributions: Conceptualization, C.X. and X.L.; methodology, C.X.; software, J.Q.; formal analysis, W.M.; investigation, J.M.; resources, P.G.; data curation, C.X.; writing—original draft preparation, C.X.; writing—review and editing, D.D. and B.Y.; visualization, B.Y.; supervision, D.D. and B.Y.; project administration, D.D. and B.Y.; funding acquisition, D.D. and B.Y. All authors have read and agreed to the published version of the manuscript.

Funding: This research was funded by the National Natural Science Foundation of China (No. 12274451), National Key Research and Development Program of China (No. 2021YFF0700303, No. 2022YFE0100700), China Postdoctoral Science Foundation (2022M713338), Key Research and Development Program of Shaanxi Province (2022GY-083), and Open Research Fund for development of high-end scientific instruments and core components of the Center for Shared Technologies and Facilities, XIOPM, CAS (SJZ1-202206001).

Institutional Review Board Statement: Not applicable.

Informed Consent Statement: Not applicable.

Data Availability Statement: Not applicable.

Acknowledgments: We thank Chen Bai at University of Chinese Academy of Sciences for his comments and suggestions on this article.

Conflicts of Interest: The authors declare no conflict of interest.

References

1. Breuninger, T.; Greger, K.; Stelzer, E.H.K. Lateral modulation boosts image quality in single plane illumination fluorescence microscopy. *Opt. Lett.* **2007**, *32*, 1938–1940. [CrossRef] [PubMed]
2. Planchon, T.A.; Gao, L.; Milkie, D.E.; Davidson, M.W.; Galbraith, J.A.; Galbraith, C.G.; Betzig, E. Rapid three-dimensional isotropic imaging of living cells using Bessel beam plane illumination. *Nat. Methods* **2011**, *8*, 417–423. [CrossRef] [PubMed]
3. Dan, D.; Gao, P.; Zhao, T.Y.; Dang, S.P.; Qian, J.; Lei, M.; Min, J.W.; Yu, X.H.; Yao, B.L. Super-resolution and optical sectioning integrated structured illumination microscopy. *J. Phys. D Appl. Phys.* **2021**, *54*, 074004. [CrossRef]
4. Thomas, B.; Momany, M.; Kner, P. Optical sectioning structured illumination microscopy with enhanced sensitivity. *J. Opt.* **2013**, *15*, 094004. [CrossRef]
5. Isobe, K.; Takeda, T.; Mochizuki, K.; Song, Q.Y.; Suda, A.; Kannari, F.; Kawano, H.; Kumagai, A.; Miyawaki, A.; Midorikawa, K. Enhancement of lateral resolution and optical sectioning capability of two-photon fluorescence microscopy by combining temporal-focusing with structured illumination. *Biomed. Opt. Express* **2013**, *4*, 2396–2410. [CrossRef]
6. Paddock, S.W. Confocal laser scanning microscopy. *Biotechniques* **1999**, *27*, 998–1002. [CrossRef]
7. Amos, W.B.; White, J.G. How the Confocal Laser Scanning Microscope entered Biological Research. *Biol. Cell* **2003**, *95*, 335–342. [CrossRef]
8. Denk, W.; Strickler, J.H.; Webb, W.W. Two-photon laser scanning fluorescence microscopy. *Science* **1990**, *248*, 73–76. [CrossRef]
9. Wu, J.L.; Liang, Y.J.; Chen, S.; Hsu, C.L.; Chavarha, M.; Evans, S.W.; Shi, D.Q.; Lin, M.H.Z.; Tsia, K.K.; Ji, N. Kilohertz two-photon fluorescence microscopy imaging of neural activity in vivo. *Nat. Methods* **2020**, *17*, 287–290. [CrossRef]
10. Vettenburg, T.; Dalgarno, H.I.C.; Nylk, J.; Coll-Llado, C.; Ferrier, D.E.K.; Cizmar, T.; Gunn-Moore, F.J.; Dholakia, K. Light-sheet microscopy using an Airy beam. *Nat. Methods* **2014**, *11*, 541–544. [CrossRef]
11. Stelzer, E.H.; Strobl, F.; Chang, B.-J.; Preusser, F.; Preibisch, S.; McDole, K.; Fiolka, R. Light sheet fluorescence microscopy. *Nat. Rev. Methods Prim.* **2021**, *1*, 73. [CrossRef]
12. Neil, M.A.A.; Juskaitis, R.; Wilson, T. Method of obtaining optical sectioning by using structured light in a conventional microscope. *Opt. Lett.* **1997**, *22*, 1905–1907. [CrossRef] [PubMed]
13. O'Holleran, K.; Shaw, M. Optimized approaches for optical sectioning and resolution enhancement in 2D structured illumination microscopy. *Biomed. Opt. Express* **2014**, *5*, 2580–2590. [CrossRef]
14. Ilie, M.A.; Caruntu, C.; Lupu, M.; Lixandru, D.; Tampa, M.; Georgescu, S.R.; Bastian, A.; Constantin, C.; Neagu, M.; Zurac, S.A.; et al. Current and future applications of confocal laser scanning microscopy imaging in skin oncology. *Oncol. Lett.* **2019**, *17*, 4102–4111. [CrossRef] [PubMed]
15. Huisken, J.; Swoger, J.; Del Bene, F.; Wittbrodt, J.; Stelzer, E.H.K. Optical sectioning deep inside live embryos by selective plane illumination microscopy. *Science* **2004**, *305*, 1007–1009. [CrossRef] [PubMed]
16. Voie, A.H.; Burns, D.; Spelman, F. Orthogonal-plane fluorescence optical sectioning: Three-dimensional imaging of macroscopic biological specimens. *J. Microsc.* **1993**, *170*, 229–236. [CrossRef] [PubMed]
17. Gu, S.Y.; Yu, X.H.; Bai, C.; Min, J.W.; Li, R.Z.; Yang, Y.L.; Yao, B.L. Multiple airy beams light-sheet fluorescence microscopy. *Front. Phys.* **2022**, *10*, 1360. [CrossRef]
18. Dan, D.; Yao, B.L.; Lei, M. Structured illumination microscopy for super-resolution and optical sectioning. *Chin. Sci. Bull.* **2014**, *59*, 1291–1307. [CrossRef]

19. Gustafsson, M.G.L.; Shao, L.; Carlton, P.M.; Wang, C.J.R.; Golubovskaya, I.N.; Cande, W.Z.; Agard, D.A.; Sedat, J.W. Three-dimensional resolution doubling in wide-field fluorescence microscopy by structured illumination. *Biophys. J.* **2008**, *94*, 4957–4970. [CrossRef]
20. Li, X.S.; Wu, Y.C.; Su, Y.J.; Rey-Suarez, I.; Matthaeus, C.; Updegrove, T.B.; Wei, Z.; Zhang, L.X.; Sasaki, H.; Li, Y.; et al. Three-dimensional structured illumination microscopy with enhanced axial resolution. *Nat. Biotechnol.* **2023**. [CrossRef]
21. Wilson, T. Optical sectioning in fluorescence microscopy. *J. Microsc.* **2011**, *242*, 111–116. [CrossRef] [PubMed]
22. Tkaczyk, T.S.; Rahman, M.; Mack, V.; Sokolov, K.; Rogers, J.D.; Richards-Kortum, R.; Descour, M.R. High resolution, molecular-specific, reflectance imaging in optically dense tissue phantoms with structured-illumination. *Opt. Express* **2004**, *12*, 3745–3758. [CrossRef] [PubMed]
23. Schaefer, L.H.; Schuster, D.; Schaffer, J. Structured illumination microscopy: Artefact analysis and reduction utilizing a parameter optimization approach. *J. Microsc.* **2004**, *216*, 165–174. [CrossRef] [PubMed]

Disclaimer/Publisher's Note: The statements, opinions and data contained in all publications are solely those of the individual author(s) and contributor(s) and not of MDPI and/or the editor(s). MDPI and/or the editor(s) disclaim responsibility for any injury to people or property resulting from any ideas, methods, instructions or products referred to in the content.